
Co-Registration of Intra-Operative Brain Surface Photographs and Pre-Operative MR Images

Benjamin Berkels¹ · Ivan Cabrilo² · Sven Haller³ · Martin Rumpf⁴ · Karl Schaller²

Published in International Journal of Computer Assisted Radiology and Surgery
Author's version. The final publication is available at link.springer.com

<http://link.springer.com/article/10.1007/s11548-014-0979-y>

Abstract *Purpose:* Brain shift, the change in configuration of the brain after opening the dura mater, is a significant problem for neuronavigation. Brain structures at intra-operative deformed positions must be matched with corresponding structures in the pre-operative 3D planning data. A method to co-register the cortical surface from intra-operative microscope images with pre-operative MRI segmented data was developed and tested.

Methods: Automated classification of sulci on MRI extracted cortical surfaces was tested by comparison with user guided marking of prominent sulci on an intra-operative photography. A variational registration method with a fidelity energy for 3D deformations of the cortical surface in conjunction with a higher order, linear elastic prior energy was used for the actual registration. The minimization of this energy was performed with a regularized gradient descent scheme using finite elements for spatial discretization. The sulcal classification method was tested on eight different clinical MRI data sets by comparison of the deformed MRI scans with intra-operative photographs of the brain surface.

Results: User intervention was required for marking sulci on the photos demonstrating the potential for incorporating an automatic classifier. The actual registration was validated first on an artificial testbed. The complete algorithm for the co-registration of actual clinical MRI data was successful for eight different patients.

Conclusions: Pre-operative MRI scans can be registered to intra-operative brain surface photographs using a surface-to-surface registration method. This co-registration method has potential applications in neurosurgery, particularly during functional procedures.

Keywords: elastic registration, brain segmentation, sulci, variational methods, surface classification, cortical surface tracking

¹Aachen Institute for Advanced Study in Computational Engineering Science (AICES), RWTH Aachen University, Schinkelstr. 2, 52062 Aachen, Germany · ² Department of Neurosurgery, University Hospitals of Geneva and Faculty of Medicine of the University of Geneva, Gabrielle-Perret-Gentil 4, 1205 Genève, Switzerland · ³ Department of Imaging and Medical Informatics, University Hospitals of Geneva and Faculty of Medicine of the University of Geneva, Gabrielle-Perret-Gentil 4, 1205 Genève, Switzerland · ⁴Institut für Numerische Simulation, Rheinische Friedrich-Wilhelms-Universität Bonn, Endenicher Allee 60, 53115 Bonn, Germany

1 Introduction

The improvement of image guided surgical navigation relies on advances in medical imaging. In particular, the development of novel efficient and robust co-registration methodology in image processing quickly triggered intense interest from the medical world to translate this progress on the imaging side to novel navigation tools with a strong impact on the improvement of clinical diagnostics and treatment planning. The acquisition of high quality images and co-registration of different imaging modalities have come to represent an essential element of pre-operative planning, intra-interventional navigation, as well as post-treatment follow-up. Achievements in co-registration have given rise to further development and application in most, if not all, interventional medical fields.

A particular challenge is the fusion of images of different dimensionality. It is comparably easy to record pre-operative 3D data, whereas mostly only 2D images are easily accessible during the surgical intervention. Thus, even though technically demanding, the fusion of 2D and 3D image data is a fundamental task in image-guided medical intervention. Markelja et al. [15] survey approaches for the registration of pre-operative volumetric CT or MRI data with intra-operative 2D X-ray projection images. Burschka et al. [6] present a method to register CT scans to endoscopic images by a 3D reconstruction of the 2D images followed by a registration of the reconstruction to the CT data. The use of 2D views for pose estimation of a pre-surgical 3D image has been investigated in [9]. A variational approach is proposed in [12] for the matching of 3D CT data to 2D ultrasound slices that, unlike other volume-to-slice approaches, only uses the given data and relies on a higher order regularization. A method for the matching of photos of human faces with 3D surface models extracted from MRI data using rigid deformations has been suggested in [8]. Recently, a registration method for sparse but highly accurate 3-D line measurements with a surface extracted from volumetric planning data based on the consistent registration idea and higher order regularization was introduced in [2, 4].

The matching of photographic images with pre-operative MRI data is a particular challenge in cranial neuronavigation. Such a tool integration in the navigation software would allow the neurosurgeon to *intra-operatively* confirm the borders of the work-field on pre-operative image data sets, as well as to identify neighboring anatomical structures of importance and to verify extent of resection. In the context of intracranial electroencephalography, the photograph–MRI registration problem has been investigated via a control point matching approach in [10]. Recently, normalized mutual information has been applied for the rigid co-registration of brain photographs and MRI extracted cortical surfaces [22]. A major limitation of note, however, is that due to the brain shift the surgeon’s view of the operating site is not in a rigid transformation correspondence to pre-operative images. Indeed, standard intracranial neuronavigation devices do not correct for this movement of brain [18].

The main contributions of this paper are twofold:

- Firstly, a new classification method for crease pattern on implicit surfaces is presented and its application to the classification of sulci on implicit level set representations of cortical surfaces is discussed.

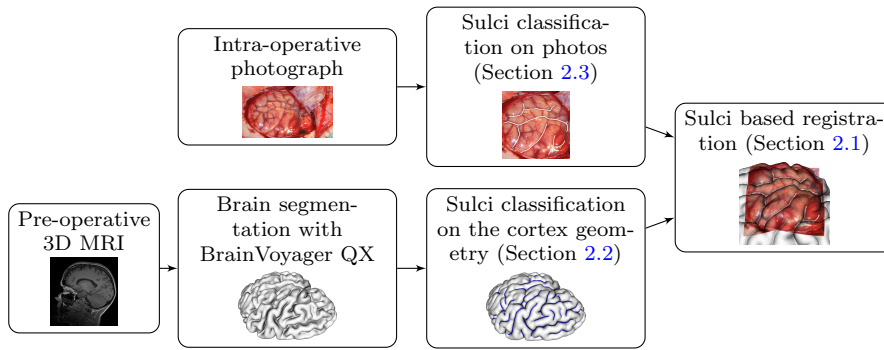


Figure 1 A flowchart describing the interplay of the different algorithmic ingredients of our approach.

- Secondly, a novel 2D-3D surface registration method is proposed, where a non-rigid 3D deformation of a graph representation of a cortical surface to match user marked sulci on a 2D brain photograph is computed.

A first version of this approach has first been briefly sketched in [5]. Different from [5], the underlying registration algorithm presented here is improved concerning the handling of the region of interest on the photos. Furthermore, we give a detailed description of all aspects of the method here. In particular, we give here a theoretical motivation for the surface classification method (cf. Section 2.2). Furthermore, the actual registration algorithm is described in a separate section (cf. Section 3). Finally, we evaluate the method on eight clinical cases and give a detailed qualitative and quantitative discussion of the results on the background of the potential clinical application. A flow chart describing the algorithm is given in Figure 1. The paper is organized as follows. In Section 2, the different ingredients of the co-registration method are presented. At first, prior and fidelity terms of the registration energy are derived in Section 2.1. The underlying sulci classification on the 3D geometry and on the brain photos are discussed in Sections 2.2 and 2.3, respectively. Section 3 investigates the different components for the resulting algorithm, with a description of a finite element scheme for the minimization of the energy in 3.1 and the sulci classification scheme on the cortex geometry in Section 3.2. The actual application to different clinical cases is presented in Section 4 together with a discussion of the results and the limitations of the approach. Finally, in Section 6 we draw conclusions and mention interesting directions of future investigations including the incorporation of a discriminative dictionary algorithm to support the clinician in the sulci classification on photos.

2 Setting up a variational method

The aim of this paper is to register a photograph of the exposed human cortex with the cortex geometry extracted from an MRI data set (cf. Figure 2) using the sulci as fiducials. The 2D digital photographs were taken intra-operatively after supratentorial craniotomy and durotomy, and before corticotomy, using a digital camera (*Fujifilm Finepix Real 3D, Digital Camera W3*: 10 MegaPixels Twin-CCD,

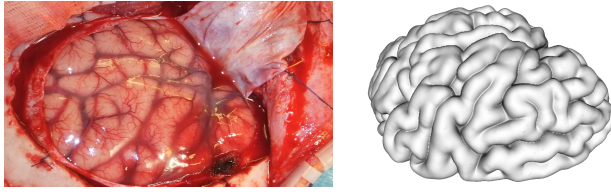


Figure 2 Input data of the algorithm: on the left a photograph after supratentorial craniotomy, on the right the cortical surface extracted from an MRI.

3x Fujinon Optical Zoom Twin-Lens (Tokyo, Japan)) positioned approximately 20 cm above the craniotomy at a typical microscope location. Lighting was adjusted to reduce reflections, so that all surface features appear clearly on the photo. The MR imaging was performed on a 3T MRI scanner. T1-weighted MPRAGE/MP2RAGE sequences ($1 \times 1 \times 1 \text{ m}^3$, $256 \times 256 \times 176$ matrix) were segmented into gray and white matter using BrainVoyager QX [11] and then converted into signed distance functions of the cortical surface using a fast marching method (see Section 3.2 and Figure 11). The ingredients of the proposed approach are a sulci classification on the cortex geometry (Section 2.2) and on the photograph (Section 2.3), and a variational approach to describe the co-registration as a minimization problem on a suitable energy defined on deformations of the cortical surface (Section 2.1). In what follows, we will at first assume that the sulci classifications both on the photography and on the cortical surface are given via thin region marking and derive the variational approach.

2.1 An energy functional to estimate classifier correspondences

The co-registration of an MRI extracted cortical surface $\mathcal{C} \subset \mathbb{R}^3$ and a photograph to compensate for deformation effects such as the brain shift is based on a co-registration of the sulci classifiers on \mathcal{C} and on the photograph. To this end, we suppose \mathcal{C} to be described as a graph surface, described by a graph function z over a two dimensional parameter domain ω , i. e.

$$\mathcal{C} = \{(x, z(x)) \in \mathbb{R}^3 | x \in \omega\}$$

with parameter domain $\omega \subset \mathbb{R}^2$ and graph function $z : \omega \rightarrow \mathbb{R}$. We are interested in a local registration of the region described by the craniotomy, where such a graph representation can be easily derived from the signed distance function used in Section 2.2. This conversion is computed in a preprocessing step (for details we refer to Section 3.2). Furthermore, let g denote a function of the image domain Ω of the photo with $g \in L^\infty(\Omega)$, which is considered as a given sulci classifier on the photographic plane (cf. Section 2.3), and let $f \in L^\infty(\omega)$ be the corresponding classifier on the cortical surface given as a function on the parameter domain ω . We suppose that both classifier functions map into the unit interval $[0, 1]$ and they are assumed to be close to 1 in the central region of the sulci and close to 0 outside. These classifiers will be defined in Section 2.2 and 2.3 and represent comparably thin stroke type pattern on the graph domain and the photographic plane respectively.

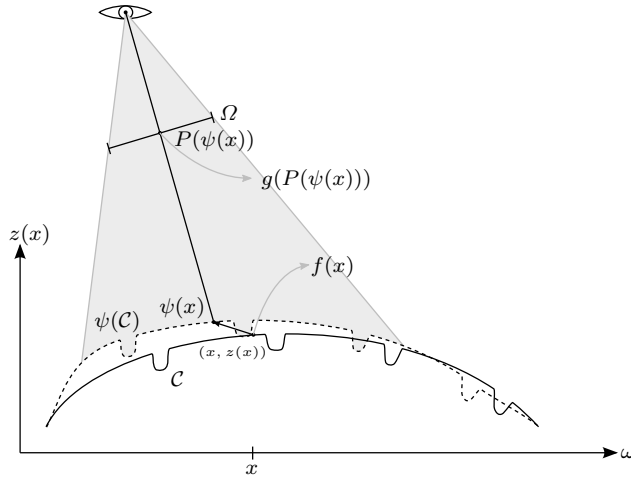


Figure 3 A schematic sketch of the camera projection of the deformed graph $\psi(\mathcal{C})$ of the cortical surface \mathcal{C} defined over the graph domain ω onto the camera plane Ω . On the camera plane the sulci classifier g is defined and can be evaluated at the deformed and projected position $P(\psi(x))$. This value is compared in the fidelity energy E_{match} with the sulci classifier f from the cortical surface given as a function on the graph domain ω .

Finally, we denote by $P : \mathbb{R}^3 \rightarrow \Omega$ the mapping which represents the projection of points in \mathbb{R}^3 onto the image plane Ω derived from known camera parameters and estimated parameters of the camera position. Let us remark that we thereby implicitly rule out self occlusions of the graph surface \mathcal{C} under the image plane projection. To eliminate the need for rotations in the projection, we assume that \mathcal{C} was already rotated to fit the approximate viewing direction of the photo with $(0, 0, 1)^T$ being the viewing direction, cf. end of Section 4 for more details on how the viewing direction can be fitted. The projection typically is either a simple orthogonal projection, i.e. $P(y) = (y_1, y_2)$ for $y \in \mathbb{R}^3$ or, more realistically, a perspective projection: For a camera position $c \in \mathbb{R}^3$ and a focal length $d_f > 0$, the perspective projection of $y \in \mathbb{R}^3$ is

$$P(y) = \frac{d_f}{(y_3 - c_3)}(y_1 - c_1, y_2 - c_2) + (c_1, c_2).$$

Note that the matrix encoding the orientation of the camera is the identity matrix since \mathcal{C} was rotated to fit the approximate viewing direction. Thus, this matrix vanishes from the projection formula.

Now, we ask for a deformation of the graph surface, which is described by a vector valued function $\psi : \omega \rightarrow \mathbb{R}^3$ defined on the parameter domain ω of the graph function z that matches $(x, z(x)) \in \mathcal{C}$ to a deformed position $\psi(x)$, cf. Figure 3. If $\psi(\mathcal{C})$ is a proper representation of the actual, intra-interventional position of the cortical surface \mathcal{C} , then we expect that sulci detected on \mathcal{C} and represented by the classifier f on ω are mapped onto sulci marked on the photographic domain Ω via the classifier g . Thereby, matching should ensure a coincidence of the surface classifier $f(x)$ on the MRI described cortical surface and the image classifier g evaluated at the projected deformed position $P(\psi(x))$ for all x on the parameter domain ω , i.e. $(g \circ P \circ \psi)(x) \approx f(x)$ for all $x \in \omega$. Furthermore, it is important

to take into account that the photo only shows a subset of the cortical surface \mathcal{C} . Thus, there will be sulci detected on \mathcal{C} that have no correspondences on the photo. We design a data term to allow sulci on \mathcal{C} without correspondences on the photo by using the factor $(1 - f(x))$. This factor vanishes when $f = 1$, i. e. on sulci detected on \mathcal{C} . Thus, proper matching can be encoded via the minimization of the matching energy

$$E_{\text{match}}[\psi] = \frac{1}{2} \int_{\omega} [(1 - f(x))(g(P(\psi(x))) - f(x))]^2 A(x) dx$$

based on a surface integral over \mathcal{C} with the area element $A(x) = (1 + |\nabla z(x)|^2)^{\frac{1}{2}}$, to consistently reflect the cortex geometry. Indeed, the energy is small if the classifier on the photo at the deformed and projected position coincides with the classifier on the graph surface ($(g \circ P \circ \psi)(x) \approx f(x)$). This coincidence is relevant only apart from classified sulci on the graph surface, where $f(x) = 1$. Minimization of this energy is a highly ill-posed problem. Not only the deformation component in the plane of the graph is underdetermined as in usual 2D to 2D registration problems, but due to the 2D to 3D character of our model, the height variation of the graph is an additional pointwise degree of freedom. Hence, in the overall variational approach the matching energy is complemented by a suitable elastic regularization energy, which acts as a smoothing prior on admissible deformations ψ . Here, we consider the cortical surface as a thin elastic structure and choose as a regularizing prior the second order, elastic thin plate spline energy

$$E_{\text{reg}}[\psi] = \frac{1}{2} \int_{\omega} |\Delta\psi_1(x)|^2 + |\Delta\psi_2(x)|^2 + |\Delta\psi_3(x) - \Delta z(x)|^2 dx$$

which in particular measures in a (linearized sense) the bending energy of the cortical surface \mathcal{C} under the deformation ψ . Here, Δ denotes the Laplace operator. As long as ψ is locally just an affine deformation, it does not contribute to the energy. Indeed, E_{reg} is rigid body motion invariant (cf. [16]). To strongly bend the surface a deformation with large second derivatives is required, which is associated with large terms $\Delta\psi_i$. Note that a simple first order regularization like the Dirichlet energy $\frac{1}{2} \int_{\omega} |\nabla(\psi_1(x) - x_1)|^2 + |\nabla(\psi_2(x) - x_2)|^2 + |\nabla(\psi_3(x) - z(x))|^2 dx$ of the displacement $\psi - (\cdot, z(\cdot))$ is not sufficient since matching information is mostly given on a low dimensional subset where a proper extrapolation is required and the Dirichlet energy does not reflect surface bending. Finally, we combine the matching energy E_{match} (fidelity energy) and the regularization energy E_{reg} (prior) to the total energy functional

$$E[\psi] = E_{\text{match}}[\psi] + \lambda E_{\text{reg}}[\psi]$$

on deformations ψ defined on the parameter domain ω encoding the deformation of the cortical surface \mathcal{C} , where λ is a positive constant controlling the strength of the regularization. For all registration results shown in this paper we have used the same value of λ , i. e. $\lambda = 10^{-4}$. Our registration method is now based on a minimization of the functional E . The corresponding algorithm is described in Section 3.1.

As first test for the performance of our co-registration approach we artificially generated test data as follows. For an MRI extracted cortical surface we generated an image by applying a nonrigid deformation on the graph created from the

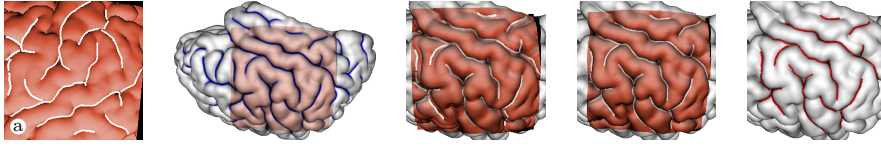


Figure 4 Results of the co-registration method are displayed for a test data pair of simulated photograph and an MRI extracted cortical surface. From left to right: the photograph with the manual marking of sulci / the cortical surface extracted from the MRI with classified sulci marked in blue and the photograph rendered transparently at the appropriate location on the surface / a zoom at the region of interest showing the initial mismatch of sulci in the photograph and on the cortical surface / the same zoom view after the co-registration / the co-registered sulci marking from the photo plotted in red on the cortical surface.

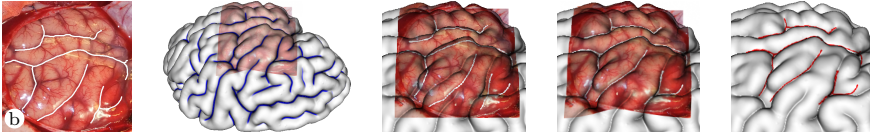


Figure 5 Results of the co-registration method for a pair of a true photograph and an MRI extracted cortical surface displayed as in Figure 4.

cortical surface and then using a given projection to map the classification on the graph to the camera plane. Then this projected image is considered as the input photograph and sulci have been marked on it by hand. The pair of input data together with the computed registration result are depicted in Figure 4. Figure 5 depicts results obtained via a minimization of the functional $E[\cdot]$ for a clinical data set. A comprehensive discussion of the results shown in Figure 5 together with results of other case studies is given in Section 4.

2.2 A sulci classifier on the cortex geometry

In this section, we describe how to classify creases on the contour surface of a 3D object $\mathcal{B} \subset D$ represented via its signed distance function $d : D \rightarrow \mathbb{R}$ on a computational domain $D \subset \mathbb{R}^n$ where $n = 2$ or 3 . In the application, the object is a brain volume and the creases are the sulci on the cortical surface. We aim for a moment based analysis of the (cortical) surface \mathcal{C} , which is considered as the boundary of the brain domain \mathcal{B} ($\mathcal{C} := \partial\mathcal{B}$) and define the zero moment shift of the implicit surface \mathcal{C} as

$$M_\epsilon^0[\mathcal{B}](x) = \int_{B_\epsilon(x)} d(y)(y-x) dy,$$

where $B_\epsilon(x)$ denotes the ball of radius ϵ around the point x . $M_\epsilon^0[\mathcal{B}](x)$ measures how far the center of brain mass in the ball $B_\epsilon(x)$ is shifted away from the position x . To motivate the use of $M_\epsilon^0[\mathcal{B}](x)$ as a classifier for creases we consider a simple 2D example: For $a > 0$ let \mathcal{B} be a square with edge length $2a$, i. e. $\mathcal{B} = [-a, a]^2$. In this case, the corresponding signed distance function in the vicinity of the corner

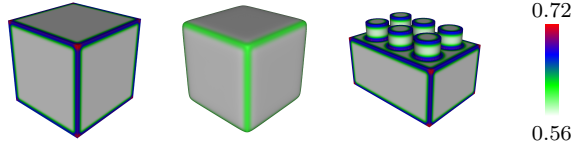


Figure 6 Moment-based classification for simple artificial shapes. Note that the cube shown on the left has sharp edges and corners whereas the edges and corners of the cube in the middle are rounded. This leads to significantly different colors showing that the proposed method is able to distinguish sharp from round edges.

(a, a) of the square \mathcal{B} is

$$d(x) = \begin{cases} |x - (a, a)| & x \in R_{\epsilon, 0, \frac{\pi}{2}}((a, a)) \\ x_2 - a & x - (a, a) \in R_{\frac{\pi}{2}, \frac{5\pi}{4}}((a, a)) \\ x_1 - a & x - (a, a) \in R_{\frac{5\pi}{4}, 2\pi}((a, a)) \end{cases}$$

where $R_{\epsilon, \alpha_1, \alpha_2}$ denotes the circular sector

$$R_{\epsilon, \alpha_1, \alpha_2}(x) := \{x + (r \cos(\phi), r \sin(\phi)) : r \in [0, \epsilon], \phi \in [\alpha_1, \alpha_2]\}.$$

Using $\int_{B_\epsilon((a,a))} d(y)(y - (a, a)) dy = \int_{B_\epsilon(0)} d(y + (a, a))y dy$ and splitting $B_\epsilon(0)$ into the three circular sectors $R_{\epsilon, 0, \frac{\pi}{2}}(0)$, $R_{\epsilon, \frac{\pi}{2}, \frac{5\pi}{4}}(0)$ and $R_{\epsilon, \frac{5\pi}{4}, 2\pi}(0)$ one obtains

$$\int_{B_\epsilon((a,a))} d(y)(y - (a, a)) dy = \frac{\epsilon^4}{4}(1, 1) + \frac{\epsilon^4}{16} \left(-1, \frac{3}{2}\pi - 1\right) + \frac{\epsilon^4}{16} \left(\frac{3}{2}\pi - 1, -1\right).$$

From this one obtains by straightforward evaluation

$$\left\| M_\epsilon^0[\mathcal{B}](a, a) \right\| = \left\| \int_{B_\epsilon((a,a))} d(y)(y - (a, a)) dy \right\| \approx 0.1889\epsilon^2.$$

Similarly, one shows $\|M_\epsilon^0[\mathcal{B}](0, a)\| = 0.25\epsilon^2$. Therefore, M_ϵ^0 can clearly distinguish between the corner (a, a) and the point $(0, a)$ on the straight part of the edge of \mathcal{B} .

In general, $\|M_\epsilon^0[\mathcal{B}](\cdot)\|$ is larger in flat regions of \mathcal{C} than in edge regions and even smaller near corners (a related moment based classification for triangulated surfaces instead of implicit surfaces and also taking into account higher order moments was introduced in [7]). Using the function $\mathcal{G}_\beta(t) = \frac{1}{1+\beta t^2}$ known from edge classification in the context of anisotropic diffusion [17], we define the scalar classification

$$\mathbf{C}(x) = \mathcal{G}_\beta \left(\left\| M_\epsilon^0[\mathcal{B}](x) \right\| / \epsilon^2 \right).$$

Due to the strict monotonicity of \mathcal{G}_β and since it maps $[0, \infty)$ to $(0, 1]$, \mathbf{C} takes values in $(0, 1]$ and the smaller the value $\mathbf{C}(x)$ the flatter the region of \mathcal{C} at x . $\|M_\epsilon^0[\mathcal{B}](x)\|$ is of order ϵ^2 since both factors in the integrand, i. e. $d(y)$ and $(y - x)$, are each of order ϵ , which leads us to divide by ϵ^2 in the definition of \mathbf{C} . Figure 6 illustrates the behavior of the classifier \mathbf{C} on three simple artificial shapes while Figure 7 shows a result on a cortical surface extracted from an MR image. Note that the classification was run with the same set of parameters for all cortical surfaces ($\beta = 20$ and $\epsilon = 4h$, where h denotes the grid width) considered in

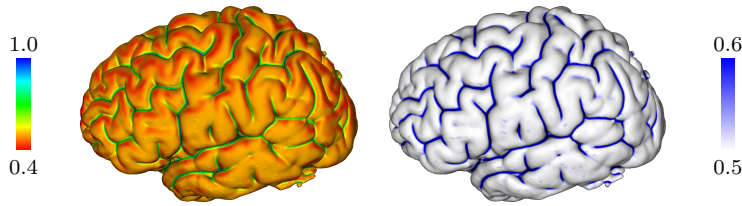


Figure 7 Moment-based classification results for a cortical surface: classifier distinguishing flat from curved regions (left), clamped classifier used for the purpose of the sulci classification (right, using simple white-to-blue color coding). The same clamped classifier visualization is used in Figures 4, 5 and 12.

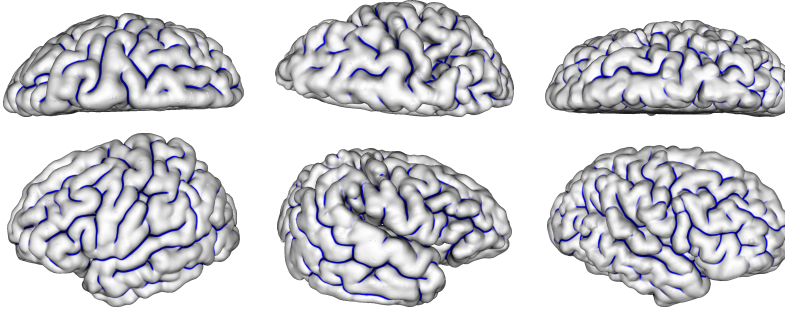


Figure 8 Different views of the classification of sulci by the new algorithm based on an implicit representation of the cortical surfaces for the cases b, g and h investigated in Section 4.

this paper allowing for a robust distinction of the surface geometry. Only for the classification of the artificial shapes in Figure 6 we used $\epsilon = 8h$ instead of $\epsilon = 4h$ to further pronounce the effects of the classifier. As shown in Figure 6, on the artificial shapes the classification allows to distinguish flat regions (white) from rounded edges (green), sharp edges (blue) and corners (red). Fig. 8 shows the obtained sulci classification for different cases to which the registration method is applied later in Section 4.

2.3 Sulci classification on photos

The classification of sulci on the photographs poses substantial difficulties, which still rule out a fully automatic classification procedure. Indeed, additional structures are frequently misinterpreted. Most prominent are cortical veins, which in addition partially occlude sulci. These veins are almost invisible in MRI in the used MP2RAGE/MP2RAGE sequences. Furthermore, reflections prevent the identification of less prominent sulci (cf. Figure 9 for a typical photograph with these difficulties being clearly vis-

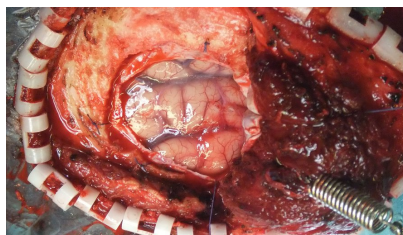


Figure 9 Cortex photograph, which shows besides the sulci also cortical veins and strong light reflections

ible (cf. Figure 9 for a typical photograph with these difficulties being clearly vis-

ible). On this background we here confine to a still manual marking of sulci by an expert who can be supported by the results of a prior automatic pre-classification of sulci based on learned discriminative dictionaries. We briefly report on this pre-classification in Section 6.2.

3 The classification and registration algorithm

In this section, we collect the ingredients of the actual implementation of our method including the multilevel finite element scheme for the energy minimization, the concrete steps of the classification algorithm of sulci on the cortex geometry and some remarks on a discriminative dictionary algorithm to support the clinician in the manual segmentation of the sulci on the photographs.

3.1 Minimizing the energy via a gradient descent finite element scheme

To minimize the objective functional we use a finite element implementation of the energy and a time discrete regularized gradient descent taking into account a suitable step size control combined with a cascadic descent approach to handle the registration in a coarse to fine manner. To implement a gradient descent method one has to evaluate the first variation $\langle E'[\psi], \phi \rangle$ of the energy E in direction of a displacement ϕ defined by

$$\langle E'[\psi], \phi \rangle := \frac{d}{dt} E[\psi + t\phi]|_{t=0}.$$

One obtains

$$\begin{aligned} \langle E'[\psi], \phi \rangle = & \int_{\omega} [(1-f)(g(P(\psi)) - f)] \nabla g(P(\psi)) \cdot DP(\psi)\phi A \\ & + \lambda(\Delta^2\psi - e_3\Delta^2z) \cdot \phi \, dx, \end{aligned}$$

where the natural boundary conditions $\partial_\nu \Delta\psi = \Delta\psi = 0$ on $\partial\omega$ for the normal ν on $\partial\omega$ are considered. Here, we have used that

$$\int_{\omega} \Delta\psi \cdot \Delta\phi \, dx = \int_{\omega} \Delta^2\psi \cdot \phi \, dx + \int_{\partial\omega} \Delta\psi \cdot \partial_\nu\phi \, da - \int_{\partial\omega} \partial_\nu\Delta\psi \cdot \phi \, da,$$

where the last two terms vanish due to the boundary conditions. The deformation ψ is initialized as the identity on \mathcal{C} , i. e. $\psi(x) = (x, z(x))$ and $e_3 = (0, 0, 1)^T$. To compute the actual descent direction, we consider a regularized gradient descent [20], which is given by the explicit update formula

$$g_\sigma(\psi^{k+1} - \psi^k, \phi) = -\tau \langle E'[\psi^k], \phi \rangle$$

for all deformation fields $\phi : \omega \rightarrow \mathbb{R}^3$. Here, $g_\sigma(\psi, \phi) := \int_{\omega} \frac{\sigma^2}{2} D\psi : D\phi + \psi \cdot \phi \, dx$ is the regularized metric ($A : B = \sum_{ij} A_{ij} B_{ij}$). In fact, the metric g_σ leads to a filtering of the classical descent direction (in the standard metric) with a filter comparable to a Gaussian filter of width σ .

For the spatial discretization we consider bilinear Finite Elements on a uniform rectangular mesh of grid size h overlaying ω . The associated lumped mass matrix M_h and stiffness matrix L_h are defined as

$$(M_h)_{ij} = \int_{\omega} \mathcal{I}_h(\varphi_i^h \varphi_j^h) dx, \quad (L_h)_{ij} = \int_{\omega} \nabla \varphi_i^h \cdot \nabla \varphi_j^h dx,$$

where \mathcal{I}_h is defined as the bilinear Lagrangian interpolation and $\{\phi_j^h\}_{j \in J_h}$ the canonical finite element basis of nodal functions with J_h being the nodal index set. If we denote by $\bar{\Psi} = (\bar{\Psi}_1, \bar{\Psi}_2, \bar{\Psi}_3)$ the nodal vector of the finite element approximation Ψ approximating the continuous deformation ψ , we obtain as the resulting approximation of the bi-Laplacian Δ^2 the matrix $\Delta_h^2 = M_h^{-1} L_h M_h^{-1} L_h$. The discrete metric reads as $G_{\sigma}(\bar{\Psi}, \bar{\Phi}) := \sum_{i=1}^3 \left(\frac{\sigma^2}{2} L_h + M_h \right) \bar{\Psi}_i \cdot \bar{\Phi}_i$. Now, one applies a numerical quadrature on each cell C of the finite element mesh to effectively evaluate the energy and the variation of the energy. Thereby, one obtains for the discrete energy

$$E_h[\Psi] = \frac{1}{2} \sum_{C \in \mathfrak{C}} \sum_{q=1}^4 w_q (1 - f(x_C^q)) (g(P(\Psi(x_C^q))) - f(x_C^q))^2 A(x_C^q) + \frac{\lambda}{2} M_h \sum_{i=1}^3 \Delta_h^2 \bar{\Psi}_i \cdot \bar{\Psi}_i.$$

Here, \mathfrak{C} denotes the set of grid cells and x_C^q the q -th quadrature point in a cell C with corresponding weight w_q for a Gauss quadrature scheme of order 3. Finally, the variation of E_h needed for the fully discrete gradient descent is given by

$$\begin{aligned} \langle E_h'[\Psi], \Phi \rangle &= \sum_{C \in \mathfrak{C}} \sum_{q=1}^4 w_q (1 - f(x_C^q)) (g(P(\Psi(x_C^q))) - f(x_C^q)) \nabla g(P(\Psi(x_C^q))) \\ &\quad \cdot DP(\Psi(x_C^q)) \Phi(x_C^q) A(x_C^q) \\ &\quad + \lambda M_h \sum_{i=1}^3 \Delta_h^2 \bar{\Psi}_i \cdot \bar{\Phi}_i. \end{aligned}$$

As step size control we use Armijo's rule with widening [1]. The energy is in general strongly non-convex. Hence, the computation of global minimizers requires special care. We choose here a multilevel minimization approach with a cascading descent from coarse to fine grids. Figure 10 shows the plots of the energy decay in the multilevel gradient descent for four different clinical data sets. The corresponding co-registration results are presented in Figure 12 and discussed in Section 4. The plots indicate a rather quick descent in the energy on every level. We start on grid level 5 with grid size 2^{-5} and proceed step wise up to grid level 8 with grid size 2^{-8} . One observes an expected increase of the matching energy due to a substantial addition of geometric details from one level to the next finer one. Correspondingly with a decay in the matching energy the regularization energy increases, which reflects the resulting increase in the complexity of the deformation. The registration method is so far not optimized with respect to speed. A standard CPU implementation with a photo resolution of 257×257 pixels and a 257×257 finite element grid for the representation of the surface graph subset that contains the region shown in the photo comes with runtimes between 18 and 63 seconds, depending on the data set. Let us emphasize that real time tracking could use results from previous frames as initialization leading to a substantial speed up. Furthermore, a GPU implementation with an expected substantial speed up is feasible.

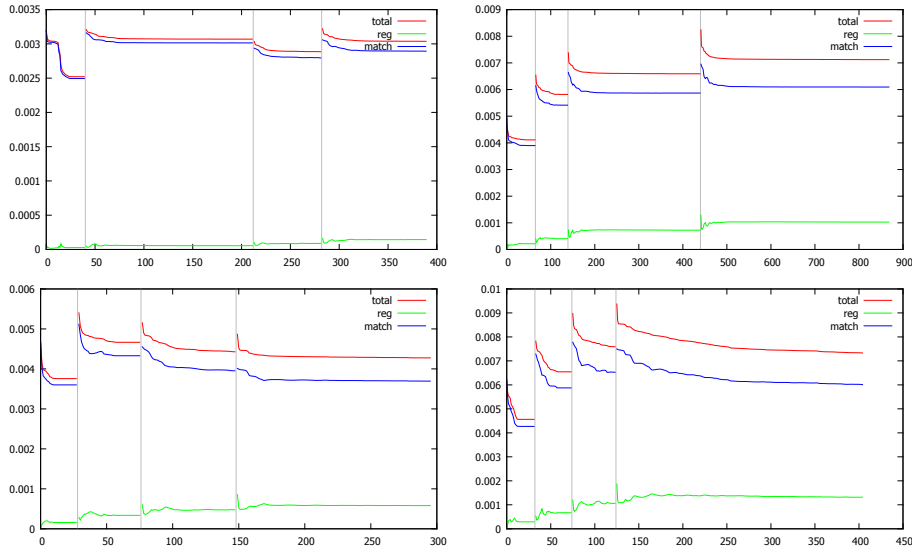


Figure 10 For the clinical data sets c-f from Figure 12 the energy decay is plotted over the iteration count in the multilevel gradient descent scheme. The different energy contributions are color coded (red: total energy E , green: regularization energy E_{reg} , blue: matching energy E_{match}) and vertical lines indicate the transition from one grid level to the next finer one.

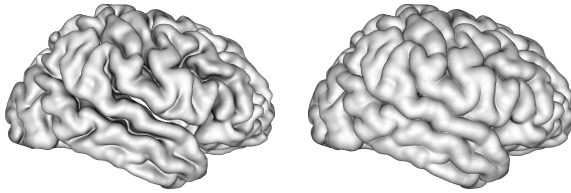


Figure 11 A cortical surface reconstructed with BrainVoyager QX (left) and the 0.01-level set of corresponding signed distance function (right).

3.2 Computing the sulci classifier on the cortex geometry

In order to use the sulci classifier for implicit surfaces discussed in Section 2.2, the triangulated surfaces generated with BrainVoyager QX need to be converted to an implicit representation. To this end, the triangulated surfaces are first rescaled and translated to fit into the unit cube and rotated to fit the approximate viewing direction of the photo. Then the signed distance function \tilde{d} of the surface is computed on a uniform rectangular grid of size 513^3 using a fast marching method [19]. Since BrainVoyager tends to underestimate the brain volume, the brain volume is “thickened” by using the 0.01-level set of \tilde{d} (cf. Figure 11). Henceforth, we consider the signed distance function $d = \tilde{d} + 0.01$ and compute the classifier \mathcal{C} in a narrow band around the 0-level set of d .

Moreover, the signed distance function $d : [0, 1]^3 \rightarrow \mathbb{R}$ is converted to a graph function $z : \omega = [0, 1]^2 \rightarrow \mathbb{R}$ as follows: For $x \in [0, 1]^2$ we set

$$z(x) = \begin{cases} \max \{z \in [0, 1] : d(x, z) = 0\} & \text{if } z \in [0, 1] \text{ with } d(x, z) = 0 \text{ exists} \\ 0 & \text{else.} \end{cases}$$

This makes use of the fact that the triangular surface was already rotated to fit the approximate viewing direction of the photo and is conceptually like putting a blanket over the surface described by the 0-level set of d from above. Since numerically d is only given on grid nodes and z is only computed on grid nodes, we use linear interpolation in the third coordinate direction to determine the zero crossings of d .

The classifier \mathbf{C} can be evaluated on $x \in \omega$ via $\mathbf{C}(x) := \mathbf{C}(x, z(x))$ using trilinear interpolation of the precomputed values of \mathbf{C} on the narrow band. Finally, we compute f by clamping \mathbf{C} to $[\cdot 5, \cdot 6]$ and rescaling the values to the unit interval $[0, 1]$. This way the sulci have a value of 1, the gyri a value of 0.

The cortex segmentation, surface classification and graph extraction is an off-line preprocessing step. Cortex triangle mesh to signed distance function conversion on a 513^3 grid takes about 5 and a half minutes, calculating the classification of the implicit surface in a narrow band around the interface takes about 22 minutes (timings for case h as an example). The runtime of the conversion of the distance function to a graph function is negligible.

4 Application to clinical data

We have applied our method to eight different clinical cases. Figure 5 already depicted results for one of these cases, whereas the remaining seven cases are considered in Figure 12.

We chose to use sulci for the co-registration process as they are generally visible brain surface structures, obviously easier to segment than gyri, and also easier to co-register. So far, and so as to allow maximum sulci co-registration, we have selected patients without gross surface signs of pathology. The 11 year-old patient shown in Figures 2 and 5 suffered of cryptogenic medication-intractable epilepsy originating in the left temporal lobe, and underwent resection of the epileptogenic region. The intra-operative photographs in the first and fifth rows of Figure 12 (cases c and g, respectively) are of a 37 year-old patient and a 23 year-old patient, respectively, also suffering from uncontrollable epilepsy originating from sclerosis of the right hippocampus. During the operations shown in these pictures, resection of this region was performed. The 51 year-old patient in the second row of Figure 12 (case d) underwent a similar operation due to the same pathology, but on the left side. The 40 and 46 year-old patients shown in the third and fourth row of Figure 12 (cases e and f), respectively, both underwent resection of left temporal epileptogenic cavernomas. Case h, in the sixth row of Figure 12, is that of a 21 year-old patient suffering from epilepsy of the right hemisphere due to Rasmussen's encephalitis. This patient underwent a right-sided trans-Sylvian functional hemispherectomy. Finally, the 20 year-old patient shown in the seventh row of Figure 12 (case i) suffered from epilepsy originating in a dysplastic right frontal lobe. During the operation shown in this photograph, right

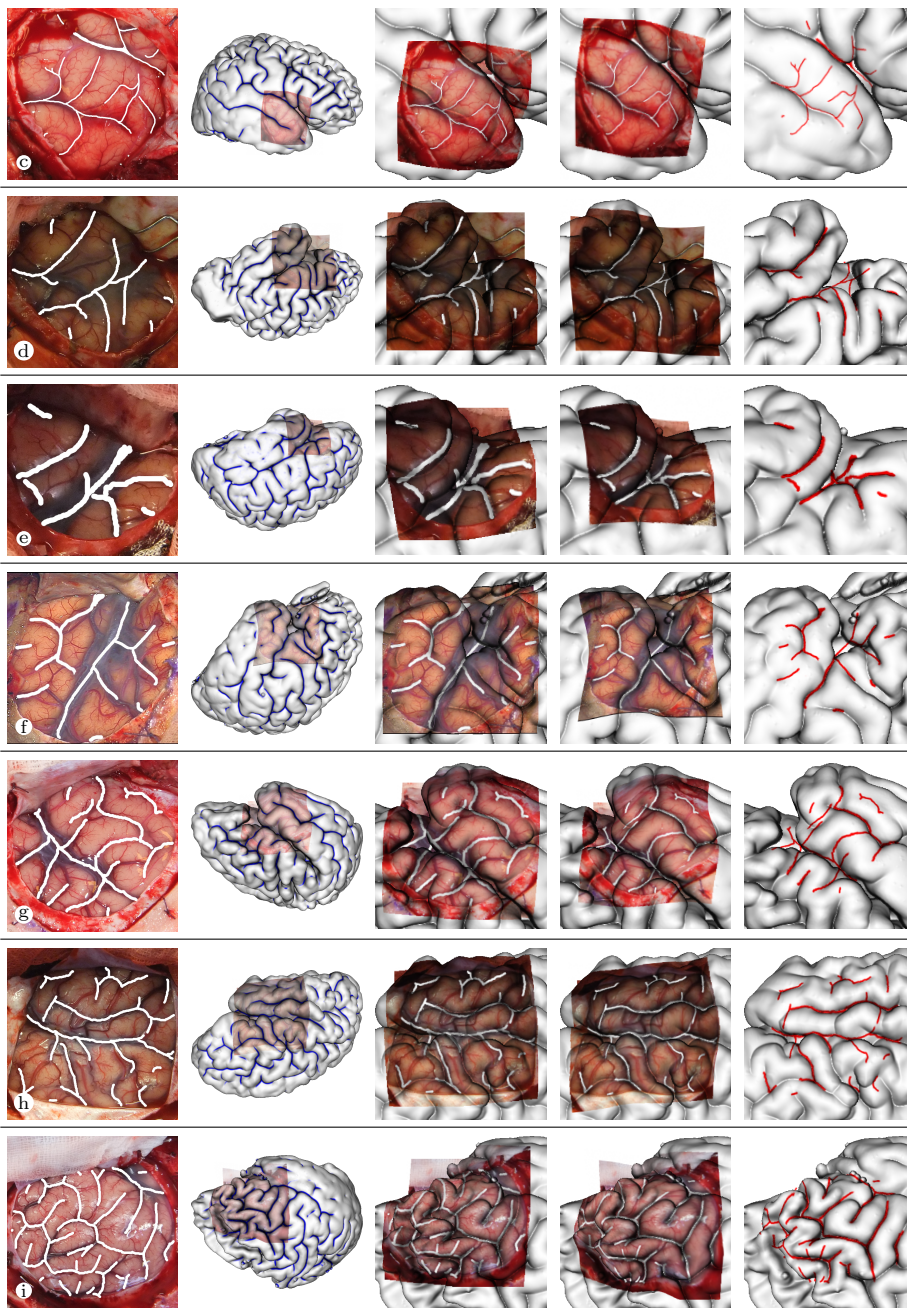


Figure 12 Results of the co-registration method are displayed row-wise for seven different clinical cases. From left to right: the photograph with the manual marking of sulci / the cortical surface extracted from the MRI with classified sulci marked in blue and the photograph rendered transparently at the appropriate location on the surface / a zoom at the region of interest showing the initial mismatch of sulci in the photograph and on the cortical surface / the same zoom view after the co-registration / the co-registered sulci marking from the photo plotted in red on the cortical surface.

frontal subdural electrode grids were placed. Intracranial electro-encephalography located with precision the epileptogenic region within the frontal lobe which was later resected during a second operation.

All photographs were taken before any dissection of the brain was performed and are seen as they would be through the operating microscope. Sulci, vessels and cortex are all identifiable.

Our technique can apply to any craniotomy of supratentorial hemispheric location, as long as sulci are visible, which is usually the case even in smaller craniotomies (first and third row of Figure 12). We used a neuronavigation workstation (KolibriTM, BrainLab, Feldkirchen, Germany) to localize the borders of the craniotomy in relation to the brain, and were therefore able to identify the exact region of interest on the reconstructed cortical surface for the co-registration. The results obtained suggest a high degree of correlation between the manually marked sulci on the photos and the cortical surfaces. As seen in the first row of Figure 12, the method properly handles sulci marked in the photo that are invisible in the reconstruction. Furthermore, as indicated in the fourth row a good correspondence of the computed smooth deformation and the true physical deformation, which appears to be smooth as well, ensures that other smaller sulci, which are not explicitly marked are also properly matched.

In its current form, our methodology requires user segmentation of sulci from intra-operative photographs. Although sulci are visible on the cortical surface, their detailed segmentation can be difficult. Firstly, certain sulci are deep-running while others are more superficial creases in the cortical blanket that can pass unseen on the 3D MRI reconstruction of the brain. Seen from above, it can be difficult to distinguish between the two (an example of this is seen in the right picture of the first row of Figure 12). Secondly, vessels coursing on the brain surface can cover portions of sulci. Thirdly, the web-like arachnoid covering of the brain can cloud out their precise trajectories. This is variable in patients and depends on age and on current or past intracranial pathology. The 37 year-old patient shown in the first row of Figure 12, the 11 year-old patient from Figure 5, the 23 year-old patient and the 20 year-old patient in the fifth and seventh rows of Figure 12 have clearly demarcated sulci, while the 51 year-old patient shown in the second row of Figure 12 has a fibrous arachnoid covering due to a previous intervention, and the sulci are therefore less distinct.

The Sylvian fissure - although a prominent region of the brain, containing vessels and arachnoid - can be difficult to segment in detail due to these last two reasons (fourth row of Figure 12). An example of this is the patient in the third row of Figure 12 where the segmentation of the Sylvian fissure is ostensibly closer to the "V" shaped segmentation (first picture from the left) than it is on the 3D MRI reconstruction (second picture from the left). Neuroanatomically speaking, the Sylvian fissure is not a sulcus, because it is not a cortical depression connecting two contiguous gyri, but rather a far larger folding, itself containing sulci and gyri in its depth. As the brain ages, its volume constitutionally - and variably - shrinks. It is therefore difficult to demarcate it with a thin line in such patients (second row of Figure 12), as compared to younger patients (Figure 5 and first, fifth, sixth and seventh rows of Figure 12). Furthermore, as can be seen in the second row of Figure 12, the Sylvian fissure in the 3D MRI reconstruction appears as an "empty" space for this reason; Co-registering this region could therefore theoretically be problematic.

| | a | b | c | d | e | f | g | h | i |
|--------|-------|-------|-------|-------|-------|-------|-------|-------|-------|
| before | 0.372 | 0.120 | 0.030 | 0.177 | 0.123 | 0.169 | 0.111 | 0.208 | 0.192 |
| after | 0.935 | 0.795 | 0.359 | 0.482 | 0.667 | 0.544 | 0.356 | 0.609 | 0.554 |

Table 1 For all investigated cases the ratio of the amount of the marked sulci on the photo which aligns with classified sulci on the cortical surface to the total amount of marked sulci on the photo is evaluated before (top row) and after (bottom row) the registration.

Finally, the reconstructed cortical surface was orientated to correspond to the incidence of the photograph to perform the co-registration. Since the intra-operative photographs were acquired with a non-neuronavigated standard digital camera, the camera parameters had to be manually estimated. Due to the inaccuracies in the manual estimation, we confined to the orthogonal projection described in Section 2.1 for the registration. In the future, we intend to address this potential bias by neuronavigating *both* the patient *and* the operating microscope, and acquiring the intra-operative photographs using the latter. In this way, optic and spatial information (coordinates of the trajectory of vision, zoom parameters) will be acquired with greater precision. In particular, this should allow us to use a more realistic perspective projection. Furthermore, the model can easily be extended to stereo images. These modifications would further improve the accuracy of the registration algorithm.

5 Discussion

A direct comparison of the manually marked sulci and the automatically segmented sulci on the deformed graph is shown for cases b, c and h in Figure 13. It underlines that sulci marked by the physician actually can be properly co-registered with the automatically segmented sulci on the cortical surfaces extracted from the corresponding MR image. In Table 1, we quantify the matching quality for all investigated cases. To this end, the ratio of the amount of the marked sulci on the photo which aligns with classified sulci on the cortical surface to the total amount of marked sulci on the photo is evaluated before and after the registration. This ratio increases substantially for all cases and thereby demonstrated the manifests of a proper matching. Nevertheless, many sulci visible on the photo still can not be reconstructed by the underlying algorithm for the extraction of cortical surfaces from MRI data, e. g. case c and case f. To further assess the effect of the registration algorithm, we compared this ratio before and after the application of our co-registration method. After confirming the normal distribution of the data according to the D’Agostino and Pearson omnibus normality test and the Shapiro-Wilk normality test, we performed a repeated measures parametric t-test, which showed a significant difference at $p < 0.0001$. With a better reconstruction – which is out of the scope of this paper – the matching quality can probably be further improved.

6 Conclusions and future work

A novel method is proposed for the registration of intra-interventional photographs (2D) taken of the cortex after a craniotomy with the cortical surface extracted

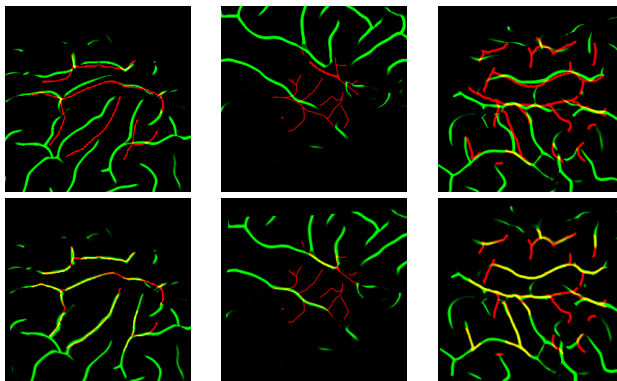


Figure 13 For cases b, c and h (left to right) the overlap of marked sulci on the photo (red) and the automatic sulci classification (green) of the undeformed (top) and the deformed (bottom) cortical surface graph is shown.

from pre-operative 3D MRI data. We presented a validation of the method on test data and for eight different clinical cases with craniotomies of different sizes. The method turns out to be effective and robust both on test and on real data, despite the previously outlined limitations, and even in the cases of smaller craniotomies, suggesting that the sulci information provided by the latter is sufficient for adequate co-registration. It is based on

- a fully automatic and robust classification of sulci on the cortical surface extracted with standard segmentation software from the MRI scan;
- on the classification of sulci on the photo, which still has to be performed manually even though dictionary based classification carries the potential to replace this by an automatic identification; and on
- the actual robust and efficient co-registration method based on a variational approach with a fidelity functional, which measures the correspondence of deformed sulci on the cortical surface and sulci on the photograph, and a thin plate spline type deformation prior.

As already discussed, the sensitivity of MRI and photography is substantially different for different anatomic structures, e.g. veins are very prominent on images yet not on the MRI modality used here. One could incorporate multiple MRI sequences and fuse vein sensitive images with the present images to improve the registration results.

Furthermore, let us emphasize that the reconstruction of the deformation component in the viewing direction from the camera is very limited. This could be substantially improved using stereo photographs of the deformed surface. In this case, we would have to consider two matching energies E_{match} , one for each camera projection.

The 3D deformation ψ of the cortical surface computed by our co-registration method, coupled to a neuronavigation interface, could therefore allow for intra-operative cortical tracking. This is of interest during neuronavigation of both structural and functional MRI. In particular, our method could help during epilepsy surgery (cf. Figure 14), where the positions of the previously placed cor-

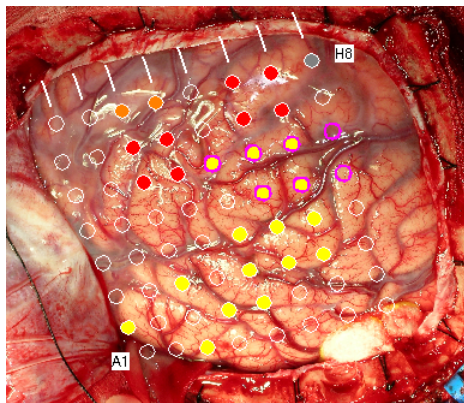


Figure 14 Intra-operative photograph of the exposed brain’s left hemisphere. Projected in color upon this photo are the locations of the various electrodes of the previously placed cortical grid used for intra-operative electro-encephalography. The obtained recordings allow to identify with greater precision the epileptogenic cortex and therefore guide surgical resection during epilepsy surgery. (image courtesy of H. Urbach, Neuroradiology, C. E. Elger, Epileptology, University Hospital Bonn)

tical electrode grid used for intracranial electroencephalography can be segmented along with the sulci and tracked as the cortex deforms.

6.1 Perspectives in neuronavigation

Although it is recognized that displacement of the cortex and deeper structures are not correlated [21], our methodology could be used to estimate to a certain degree the deformation of sub-cortical structures. To this end, the deformation ψ can be considered as boundary data for the calculation of an elastic deformation of the brain. If iterative 2D/3D registrations were performed at close and regular time intervals through automatic picture acquisition by the surgical microscope during the course of the intervention, this would allow to deform the neuronavigational 3D MR image of the brain into a perspectively current state during intervention. This could represent a solution to the brain shift of surface structures and, to a lesser degree of precision, of sub-cortical structures. As such, it could be considered to a certain extent as an alternative to intra-operative MRI [13]. Surely, this requires proper choices of the elasticity tensor in the white and grey matter and is beyond the scope of this paper.

Surgery in and around eloquent (= functionally relevant) brain areas requires visual and/or electrophysiological confirmation of the underlying cortical function. This can be achieved e. g. by direct electro-cortical stimulation, or by reliable integration of preoperatively acquired functional imaging data in the surgical plan. This is important when it comes to decision making with regard to the performance of a corticotomy without harming eloquent cortex, or where the precise placement of electrodes on the cortical surface is planned, or in case of cortical resection in epilepsy surgery. The present technique of iterative 2D/3D surface registration of digital images together with morphological 3D MRI data sets has the potential to build up a “dictionary” of the cortex of the brain at later stage, which may

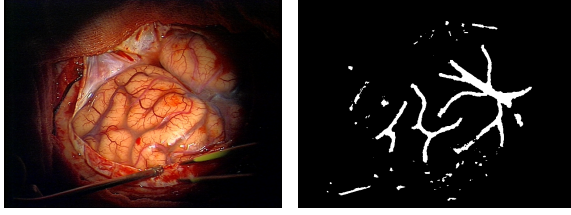


Figure 15 Photograph of the human cortex and dictionary based classification [3].

serve as a template for precise surgical planning according to functional allocation. Ultimately, the creation of such a dictionary might permit automatic recognition of brain surface features. Thereby, the brain surface, as seen through the surgical microscope might directly be co-registered to pre-interventional 3D MRI data. Such an approach would require a fast algorithmic and reliable automatic sulci recognition based on intra-operative acquisition of photos, and thus for visual orientation in real-time. For practicing neurosurgeons this could represent a major step forward in terms of intra-operative orientation, and of improvement of the intra-operative workflow, as this would allow to attain a high level of intuitive working ergonomics in combination with intra-operative safety.

6.2 Discriminative dictionary supporting the sulci classification on photos

Finally, user guidance for the identification and marking of sulci on the photos could be taken into account. A particular promising approach is based on discriminative dictionaries. The idea and key assumption behind dictionary approaches based on sparsity techniques is that a finite dimensional signal (in our case a small patch of a photograph) can be represented by a sparse linear combination of so-called *atoms*. A set of atoms is called *dictionary* and represented by a matrix $D \in \mathbb{R}^{N \times K}$ (the columns are the atoms) assuming that the signals / patches are elements of \mathbb{R}^N . Given a set of patches $Y = \{y_1, \dots, y_M\}$, a so-called *reconstructive* dictionary, is a dictionary that can represent the given patches Y with a small reconstruction error. This concept has been extended in [14] to a so-called *discriminative* dictionaries: Given two sets of patches Y_1, Y_2 that each represent a different class of patches, e.g. sulci and non-sulci, a discriminative dictionary pair D_1, D_2 has two properties. D_1 and D_2 can represent the patches Y_1 and Y_2 , respectively, with a small reconstruction error, but in addition D_2 is worse for the reconstruction of Y_1 than D_1 . The same holds for D_1 and Y_2 . The two sets Y_1 and Y_2 are obtained as follows: A set of manually marked training images is split in small overlapping patches. The patches are sorted in two sets based on the manual marking and a discriminative dictionary pair is learned from these two sets. In [3], we proposed an algorithm to solve the corresponding minimization problems and investigated the applicability of discriminative dictionaries for the classification of sulci. Figure 15 shows an example result of the discriminative dictionary approach. In the future, such a discriminative dictionary approach can be used to support the clinician in the sulci classification on photos.

Acknowledgements Benjamin Berkels and Martin Rumpf acknowledge the support by the Deutsche Forschungsgemeinschaft via the Grant Ru 567/12-1 and the Hausdorff Center for Mathematics, EXC 59. Furthermore, the authors acknowledge equipment support from Carl Zeiss (Germany). The research herein was originally started while Benjamin Berkels was at the Institute for Numerical Simulation, University of Bonn, Germany and performed in part while he was holding a visiting position at the Institute of Mathematics and Image Computing, University of Lübeck, Germany.

Conflicts of interest Benjamin Berkels, Ivan Cabrilo, Sven Haller, Martin Rumpf and Karl Schaller declare that they have no conflict of interest.

All procedures followed were in accordance with the ethical standards of the responsible committee on human experimentation (institutional and national) and with the Helsinki Declaration of 1975, as revised in 2008 (5).

Informed consent was obtained from all patients for being included in the study.

References

1. Armijo L (1966) Minimization of functions having Lipschitz continuous first partial derivatives. *Pacific Journal of Mathematics* 16(1):1–3 [11](#)
2. Bauer S, Berkels B, Ettl S, Arold O, Hornegger J, Rumpf M (2012) Marker-less reconstruction of dense 4-d surface motion fields using active laser triangulation from sparse measurements for respiratory motion management. In: *Medical Image Computing and Computer-Assisted Intervention (MICCAI 2012)*, *Lect Notes Computer Sci*, vol 7510, pp 414–421 [2](#)
3. Berkels B, Kotowski M, Rumpf M, Schaller C (2011) Sulci detection in photos of the human cortex based on learned discriminative dictionaries. In: *Scale Space and Variational Methods in Computer Vision*, *Lect Notes Computer Sci* [19](#)
4. Berkels B, Bauer S, Ettl S, Arold O, Hornegger J, Rumpf M (2013) Joint surface reconstruction and 4-D deformation estimation from sparse data and prior knowledge for marker-less respiratory motion management. *Medical Physics* *Accepted* [2](#)
5. Berkels B, Cabrilo I, Haller S, Rumpf M, Schaller K (2013) Co-registration of intra-operative photographs and pre-operative MR images. In: *Bildverarbeitung für die Medizin 2013*, Springer, pp 122–127 [3](#)
6. Burschka D, Li M, Ishii M, Taylor RH, Hager GD (2005) Scale-invariant registration of monocular endoscopic images to ct-scans for sinus surgery. *Med Image Anal* 9(5):413–426 [2](#)
7. Clarenz U, Rumpf M, Telea A (2004) Robust feature detection and local classification for surfaces based on moment analysis. *IEEE Trans Vis Comput Graph* 10(5):516–524 [8](#)
8. Clarkson MJ, Rueckert D, Hill DLG, Hawkes DJ (2001) Using photo-consistency to register 2d optical images of the human face to a 3d surface model. *IEEE Trans Pattern Anal Mach Intell* 23(11):1266–1280 [2](#)
9. Cyr CM, Kamal AF, Sebastian TB, Kimia BB (2000) 2d-3d registration based on shape matching. In: *Proc IEEE Workshop on Mathematical Methods in Biomedical Image Analysis*, pp 198–203 [2](#)

10. Dalal SS, Edwards E, Kirsch HE, Barbaro NM, Knight RT, Nagarajan SS (2008) Localization of neurosurgically implanted electrodes via photograph-mri-radiograph coregistration. *J Neurosci Methods* 174(1):106–115 [2](#)
11. Fischla B, Serenob MI, Dalea AM (1999) Cortical surface-based analysis: Ii: Inflation, flattening, and a surface-based coordinate system. *Neuroimage* 9(2):195–207 [4](#)
12. Heldmann S, Papenberg N (2009) A variational approach for volume-to-slice registration. In: *Scale Space and Variational Methods in Computer Vision*, *Lect Notes Computer Sci*, vol 5567, pp 624–635 [2](#)
13. Kuhnt D, Bauer MH, Nimsky C (2012) Brain shift compensation and neurosurgical image fusion using intraoperative mri: current status and future challenges. *Crit Rev Biomed Eng* 40:175–85 [18](#)
14. Mairal J, Bach F, Ponce J, Sapiro G, Zisserman A (2008) Discriminative learned dictionaries for local image analysis. In: *IEEE Computer Society Conference on Computer Vision and Pattern Recognition (CVPR)*, pp 1–8, DOI 10.1109/CVPR.2008.4587652 [19](#)
15. Markelja P, Tomaževića D, Likara B, Pernuša F (2012) A review of 3d/2d registration methods for image-guided interventions. *Med Image Anal* 16(3):642–661 [2](#)
16. Modersitzki J (2004) *Numerical Methods for Image Registration*. Oxford University Press [6](#)
17. Perona P, Malik J (1990) Scale-space and edge detection using anisotropic diffusion. *IEEE Trans Pattern Anal Mach Intell* 12(7):629–639 [8](#)
18. Reinges MHT, Nguyen HH, Krings T, Hütter BO, Rohde V, Gilsbach JM (2004) Course of brain shift during microsurgical resection of supratentorial cerebral lesions: limits of conventional neuronavigation. *Acta Neurochir (Wien)* 146(4):369–377 [2](#)
19. Sethian JA (1996) A fast marching level set method for monotonically advancing fronts. In: *Proc Natl Acad Sci U S A*, vol 93, pp 1591–1595 [12](#)
20. Sundaramoorthi G, Yezzi A, Mennucci A (2007) Sobolev active contours. *Int J Computer Vis* 73(3):345–366 [10](#)
21. Tharin S, Golby A (2007) Functional brain mapping and its applications to neurosurgery. *Neurosurgery* 60(4 Suppl 2):185–202 [18](#)
22. Wang A, Mirsattari SM, Parrent AG, Peters TM (2011) Fusion and visualization of intraoperative cortical images with preoperative models for epilepsy surgical planning and guidance. *Comput Aided Surg* 16(4):149–160 [2](#)